PFC/JA-87-14

# Microwave Radiation from a Tunable Circular Free Electron Laser

F. Hartemann and G. Bekefi

April 1987

# Microwave Radiation from a Tunable Circular Free Electron Laser

*F. Hartemann and G. Bekefi*

Department of Physics and Research Laboratory of Electronics,

Massachusetts Institute of Technology

Cambridge, Massachusetts, 02139

## Abstract

We report measurements of coherent microwave emission from a rotating relativistic electron ring (200 kV, 100 A, 200 ns) interacting with an azimuthally periodic wiggler magnetic field. Tunable radiation is observed between 12.5 and 18 GHz at power levels of $\sim 5$ kW. The predicted interactions occur near the crossing points of the $TM_{\ell m}$ electromagnetic waveguide modes $\omega^2 = k_{\parallel}^2 c^2 + \omega_c^2(\ell, m)$ and the beam modes $\omega = (\ell + N)\Omega_{\parallel} + k_{\parallel}v_{\parallel}$, where $\omega_c$ is the waveguide cutoff frequency, $\Omega_{\parallel}$ is the electron cyclotron frequency, $k_{\parallel}$ is the axial wavenumber, $v_{\parallel}$ is the axial drift velocity and $N$ is the number of wiggler periods. Our observations are consistent with single mode operation in the fundamental $TM_{11}$ coaxial mode.

# I. INTRODUCTION

Numerous theoretical[1] and experimental[2] studies have been carried out of free electron lasers (FEL's) in linear geometry with spatially periodic transverse or longitudinal magnetic fields. Such configurations have gain limitations imposed by the finite length of the interaction region. Recently, a novel circular version of the free electron laser has been explored both theoretically[3-9] and experimentally[10-13], in which a rotating, relativistic electron stream is subjected to an azimuthally periodic wiggler field. The potential advantages of circular FEL's as compared with the more conventional linear form are several. First, the beam circulates continuously through the wiggler field resulting in a longer effective interaction region. Second, because of the recirculation of the growing electromagnetic wave, the device provides its own internal feedback and is in essence an oscillator rather than an amplifier, as is the case in linear FEL's. Finally, because the electron motion is essentially circular, the system is very compact.

Depending on the method of production of the rotating beam, two main circular FEL configurations can be distinguished. The first configuration is the cross-field FEL configuration[3-6], in which one subjects the electrons to orthogonal electric and magnetic fields as is typical in magnetron-like devices. Here the electrons undergo a $\vec{v} = \vec{E}_r \times \vec{B}_\parallel / B_\parallel^2$ drift in a radial electric field $\hat{r}E_r$ and a uniform axial magnetic field $\hat{z}B_\parallel$. Addition of an azimuthally periodic wiggler magnetic field then results in the rippled-field magnetron[3], which has been studied previously[10]. In the alternate configuration, which is of interest in this paper, the rotating electron beam is produced by passing a hollow nonrotating electron beam through a narrow magnetic cusp[14-16]. In this manner, the $e\vec{v}_z \times \vec{B}_r$ Lorentz force at the center of the cusp effectively converts the axial beam velocity into rotational velocity downstream of the cusp region. Superimposed on the axial guiding magnetic field $\hat{z}B_\parallel$ is an azimuthally periodic wiggler field $\vec{B}_w$ generated by an assembly of samarium-cobalt bar magnets placed around the waveguide interaction region (hollow or coaxial guide, see Fig.1).

In this paper, we report detailed measurements of the operational parameters of this novel circular FEL, with special emphasis on the spectral characteristics and tunability of the device. In section II, we outline the experimental arrangement and present detailed

measurements of the rotating beam dynamics after injection through the cusp and into the wiggler magnetic field. Section III is focussed on the radiation measurements, including radiation patterns for both hollow and coaxial waveguide configurations, total power measurements for different voltage/magnetic field settings and frequency/voltage tuning curves for different magnetic fields. In section IV, these results are discussed and shown to agree well with theoretical calculations. Conclusions are drawn in section V. Our study is complementary to the recent work of Chojnacki and Destler [13] carried out at much lower voltages and currents.

## II. ROTATING BEAM DYNAMICS

The overall experimental setup is shown in Fig.1. The electron beam is generated by field emission from an annular stainless steel cathode energized directly by a Marx generator (200 kV, 15 kA, 1 $\mu$s) without a pulse forming network. The diode is immersed in a uniform axial magnetic field, with typical strengths $\sim 250$ G. The resulting hollow nonrotating beam is then passed through a sharp ( $\sim 5$ mm wide) symmetric magnetic inversion produced by a triple pole piece cusp [16]. Downstream from the cusp, the beam propagates again in the uniform guide magnetic field $\hat{z}B_{\parallel}$. Typical current/voltage characteristics are shown on Fig.2. The diode voltage remains approximately constant for $\sim 500$ ns, with the total current reaching $\sim 15$ kA. The flat top voltage is measured to an accuracy $\Delta V/V \sim 2\%$. After injection through the cusp, a square current pulse of $\sim 100$ A and $\sim 200$ ns duration propagates into the interaction region (see Fig.2). The far end of the interaction region is closed off by a $\sim 1$ cm thick plastic (Plexiglas) observation window through which all diagnostics of the electron beam and RF radiation are carried out.

Most of our experiments are carried out in the coaxial geometry illustrated in Fig.1. In this geometry the rotating electrons are perturbed by an essentially radial wiggler magnetic field. This leads to well behaved zeroth order electron orbits. However, in a few instances we remove the inner coaxial cylinder together with the inner set of wiggler magnets, thereby yielding a hollow waveguide configuration similar to that of ref. [13]. This configuration has the advantage of lowering the cutoff frequency of the fundamental coaxial waveguide mode from 12.6 GHz to 1.8 GHz for the hollow waveguide. It has the disadvantage that removal of the inner set of wiggler magnets leads to a complex wiggler field configuration

3

and electron orbit precessions [13] .

The cusp injection is characterized by a sharp threshold, which is clearly seen in the insert to Fig.3. This threshold can be readily understood. Upstream of the cusp, the nonrotating beam propagates with an axial velocity $\beta_0 c$, corresponding to the diode accelerating voltage

$$\gamma = 1 + \frac{eV}{m_0 c^2} = [1 - \beta_0^2]^{-1/2}. \tag{1}$$

After the cusp transition, the electron orbits have both axial ( $v_\parallel$ ) and azimuthal ( $v_\phi$ ) velocity components, given in terms of the upstream axial velocity by energy conservation

$$\beta_0^2 c^2 = v_\parallel^2 + v_\phi^2 = v_\parallel^2 + R^2 \Omega_\parallel^2, \tag{2}$$

where $R$ is the beam radius and $\Omega_\parallel = eB_\parallel / \gamma m_0$ . The threshold condition is defined by $v_\parallel = 0$ , and yields a threshold voltage

$$V^* = \frac{m_0 c^2}{e} \left[ \sqrt{\left(\frac{B_\parallel}{B^*}\right)^2 + 1} - 1 \right], \tag{3}$$

below which electrons are reflected at the cusp. In our experiment $B^* = m_0 c/eR \simeq 284$ G and $R = 6.0$ cm. As shown in Fig.3, we have excellent agreement between theory (solid line) and the experimental data obtained by varying the axial guide field $B_\parallel$ and measuring the threshold voltage, as indicated by the arrow on the insert of Fig.3. In addition, the aspect ratio $\alpha = v_\phi/v_\parallel$ of the helical electron orbits can be directly determined by measuring the rotation angle $\Delta\phi$ of a shadow cast into the electron stream and observed at a fixed distance $\Delta z$ on a scintillator screen [15] . For a guide field $B_\parallel = 250$ G and a beam voltage $V = 200$ kV, we measure $\alpha = R\Delta\phi/\Delta z = 2.80$ ( $\Delta\phi = 45^\circ$ , $\Delta z = 1.68$ cm), in good agreement with the theoretical value $\alpha = 2.91$ . As the diode voltage gets closer to the threshold value, $\alpha$ becomes larger and the orbits resemble more closely pure circles. Because the axial current $I_\parallel$ must be conserved, very large values of $\alpha$ (very low $v_\parallel$ ) imply a very large beam density and therefore strong self-fields. This effectively limits the aspect ratio of the orbits ; in practice, $\alpha \sim 5$ appears to be an upper bound for our experimental parameters.

The dynamics of the beam in the interaction region can be tuned by means of trimming coils embedded in the triple pole piece cusp (see Fig.1). In particular, one can minimize the

coherent off-centering mechanism discussed by Destler *et al* [14,15]. Allowing the beam to strike a blackened plexiglas plate positioned perpendicular to the propagation axis, we can photograph the Čerenkov radiation emitted [17] by the electrons and obtain a cross-section of the beam. Figure 4 shows such images of the beam obtained 5 cm into the interaction region, with and without the wiggler field. In Fig.4a, $B_w = 0$ and we observe a good quality electron ring with little energy spread ( $\Delta R/R \sim \Delta\gamma/\gamma \sim 5\%$). Fig.4b is obtained for a wiggler field with $N = 12$ periods and clearly shows a symmetric pattern with a $\phi = 30°$ period. The electron beam bunches and rotates, in very good agreement with computer simulations shown in 4d. Finally, Fig.4c illustrates our experimental results for $N = 24$, which is the periodicity used throughout our microwave measurements described below.

The wiggler magnetic field is produced [11] by an azimuthal assembly of 480 samarium-cobalt bar magnets 0.40 cm × 0.40 cm × 4.8 cm, each transversely magnetized at right angles to one of its broad faces. The remanence of our material is 9.0 kG. The wiggler amplitude at the position of the electron ring is measured to be $\sim 400$ G for the $N = 24$ periods wiggler.

## III. RADIATION MEASUREMENTS

The device is operated in the superradiant mode, where the radiation grows from noise along the helical orbit of the electron beam. Two different waveguide configurations (hollow and coaxial waveguide, with repective cutoff frequencies of 1.8 and 12.6 GHz) are used in conjunction with an $N = 24$ periods wiggler. Initial measurements of the radiation level in the 3 cm wavelength band are performed, indicating $\sim 1$ kW in the hollow waveguide configuration and $\sim 5$ kW for the coaxial structure. The higher level obtained with the coaxial waveguide probably results from the higher wiggler field strength in the interaction region for that configuration ( $\sim 400$ G). Radiation patterns are obtained by scanning the horizontal plane ($\theta$-angle) with a horn antenna and a crystal detector in the far radiation field (2 m away from the output window), while monitoring the output power with a fixed detector placed at $\theta = \theta_0$. The relative angular power distribution [ $P(\theta)/P(\theta_0)$ ] is then plotted on polar coordinates (see Figs.5,6). The total power levels can be estimated by integrating the angular distribution over the solid angle. The radiation pattern shows a

complicated structure for the hollow waveguide configuration, while it is much smoother for the coaxial waveguide, suggesting single-mode operation in the latter case. In addition, interesting results are obtained by inserting a small antenna assembly in the hollow waveguide, close to the cylindrical metal wall, and scanning azimuthally (in the vertical plane) the radially polarized component of the field, while monitoring the output power $P(\phi_0)$ with a fixed probe. The relative azimuthal power distribution, $[P(\phi)/P(\phi_0)]$ (Fig.7), shows a clear interference pattern, suggesting an $\ell = 2$ or $\ell = 4$ mode excitation. However, one must note that this measurement, involving different successive shots of the diode, implies that the azimuthal phase of the wave is not merely randomly distributed (as it should be in a perfectly axisymmetric system), but actually "locked" onto some asymetric feature of the interaction region. Such an asymmetry may well be due to a slight missalignment of the magnetic cusp or the coaxial waveguide.

Henceforth we shall confine our discussion to the coaxial waveguide configuration which yields more reproducible data at higher power levels. The relative microwave power in the 3 cm wavelength (X-band) range is measured as a function of the diode voltage for 3 different values of the guiding magnetic field $B_\parallel$ (250, 275 and 300 G). The curves shown on Fig.8 indicate that the level of radiation is barely detectable below a threshold voltage approximately equal to the cusp threshold $V^*$ . In particular, this threshold value is clearly seen to increase with $B_\parallel$ . The higher RF power levels are attained for $B_\parallel = 300$ G but the voltage range of operation is shorter. At magnetic fields below $\sim 260$ G, no high power radiation is observed in the X-band and above. This effect is related to the fact that the $(N + \ell)$ cyclotron harmonic becomes too low to excite the coaxial waveguide modes (cutoff at 12.6 GHz), and will be discussed in sec.IV.

The spatial growth (in the axial direction) of the microwave power level is measured by inserting a Ku-band waveguide/detector assembly in the gap of the coaxial waveguide oriented so as to pick up the radial polarization, and by positioning it along the $z$-axis. The origin ( $z = 0$ ) corresponds approximately to the wiggler entrance. The total power is monitored and we plot the ration $[P(z)/P(z_0)]$ in Fig.9. After a sharp onset (1–3 cm), the power level grows slowly, indicating either beam deterioration or saturation of the interaction.

The frequency of the microwave radiation is estimated first by means of high-pass waveveguide filters and found to lie in the upper X-band and in Ku-band ranges (10–20 GHz). Accurate measurements are obtained by using a 150 m long X-band dispersive line [18] . The frequency is determined by displaying the undispersed signal and the dispersed signal output on a fast oscilloscope and computing the frequency from the time difference between the two signals. The accuracy of these measurements is $\pm 10$ ns, which corresponds to a resolution of $\sim 0.6$ GHz at 12.6 GHz. The bandwidth of the microwave radiation could not be resolved with the X-band dispersive line and we thus estimate that $\Delta\omega/\omega < 5\%$. On the other hand, we note that in certain cases, the RF output pulse duration is too long, and no clean measurements could be obtained.

The radiation frequency can be changed by varying either the diode voltage $V$ or the axial magnetic field $B_{\parallel}$ ; in addition we also observe both the upshifted and the downshifted branches of the interaction, as described in section IV. Figure 10 shows the tuning curves $\omega/2\pi(V)$ obtained for 3 different values of $B_{\parallel}$ . Both high and low frequency tuning curves are clearly visible and continuous voltage tuning can be obtained from 12.5 to 18.0 GHz. The voltage operating range is seen to vary with the applied magnetic field, and the tuning curves display a threshold voltage in good agreement with both $V^{*}$ and the RF power threshold of Fig.8, at which point the high and low frequency branches merge. No deterioration of the spectral line width is observed over the full frequency tuning range. Finally, it is noteworthy that below $\sim 260$ G, no clear spectral feature can be observed while the power level decreases by more than one order of magnitude.

## IV. DISCUSSION

In this section, we first briefly review the theoretical [7−9] description of the radiative process, then analyze the experimental data within the framework of this theoretical model. In the theory, the wiggler field is assumed to be essentially radial, yielding simple electron orbits which are the combination of an axial wiggler oscillation with the unperturbed helical trajectories. The stimulated scattering process can be analyzed in terms of wave coupling. The bunched electron beam supports a so-called "synchronous mode"

$$\omega = (\ell + N)\Omega_{\parallel} + k_{\parallel}v_{\parallel}, \qquad (4)$$

7

composed both of a high harmonic cyclotron upshift and an axial Doppler upshift. Here, $\Omega_\| = eB_\|/\gamma m_0$ is the relativistic cyclotron frequency, $N$ is the number of wiggler periods, $\ell$ is the azimuthal mode number and $k_\|$ is the axial wavenumber. This beam mode can couple with a $TM_{\ell m}$ waveguide mode whose dispersion characteristics are given by

$$\omega^2 = k_\|^2 c^2 + \omega_c^2(\ell, m), \tag{5}$$

where $\omega_c(\ell, m)$ is the cutoff frequency of the $TM_{\ell m}$ mode. At the crossing points of the dispersion curves (4) and (5), both modes are synchronized in phase and one obtains energy transfer from the electron beam to the electromagnetic wave. This coupling mechanism is shown schematically in Fig.11. The output frequency of the device is

$$\omega^\pm = \gamma_\|^2(\ell + N)\Omega_\| \pm \beta_\|\gamma_\| \sqrt{\gamma_\|^2(\ell + N)^2\Omega_\|^2 - \omega_c^2(\ell, m)}, \tag{6}$$

where $\beta_\| = v_\|/c$ and $\gamma_\| = [1 - \beta_\|^2]^{-1/2}$. $\Omega_\|$, $\beta_\|$ and $\gamma_\|$ are functions of $B_\|$ and $V$ that can be derived from equations (1) and (2). Two tuning curves appear ($\pm$ sign), corresponding to the Doppler frequency upshift and downshift. The cutoff frequency $\omega_c(\ell, m)$ of the $TM_{\ell m}$ mode can be computed from the waveguide geometry (hollow or coaxial waveguide configuration).

In the case of the hollow waveguide, it is clear that one can excite a number of different $TM_{\ell m}$ modes since $N\Omega_\| >> \omega_{c0}$, where $\omega_{c0}$ denotes the cutoff frequency of the fundamental mode. This makes the analysis of the system quite complicated since no model taking into account mode competition in this device is available at the present time. Adding to the difficulty is the fact that, by removing the inner set of magnets, the electron orbits appear to be quite different [13] from those used throughout the theoretical analysis because the actual wiggler field in the hollow waveguide configuration is no longer essentially radial but also contains a strong azimuthal component. As a result, $TE$ mode excitation also becomes possible. In addition, precession effects [13] are thought to play a major role in the electron dynamics. Experimentally, both the radiation pattern (Fig.5) and the azimuthal power distribution (Fig.7) tend to confirm the high-order mode content of the microwave radiation. We also note that because one utilizes only half of the wiggler bar magnets in this configuration, the wiggler field strength is relatively small, resulting in low microwave power levels.

The coaxial configuration, on the other hand, appears to be much closer to the ideal theoretical situation. Here, the wiggler field is essentially radial at the position of the rotating electron beam and the resulting electron trajectories are well described by the theoretical model. In addition, the high cutoff frequency of the fundamental coaxial mode ($\omega_{c0}/2\pi \simeq 12.6$ GHz) ensures single mode operation. This results from the fact that we now have $N\Omega_\parallel \sim \omega_{c0}$. Indeed, the radiation pattern clearly suggests single $TM$ mode operation, with a characteristic intensity minimum on-axis (see Fig.6). The frequency/voltage tuning curves can now be compared to the theoretical predictions for $N = 24$ and $\ell = 1$. Using equation (6), we can plot the expected output frequency as a function of the diode voltage $V$ for a given value of the axial magnetic field $B_\parallel$. This is represented by the solid lines of Fig.10. The agreement with the experimental data is good. Continuous voltage tuning from 12.5 to 18.0 GHz is observed, as predicted by the theoretical model discussed above. The upshifted and downshifted tuning curves merge at the grazing intersection point, below which the synchronous wave is too slow to couple with the electromagnetic mode. Indeed, we observe a substantial decrease of the output power below the merging point (Fig.8), accompanied by the disappearance of the aforementionned narrow spectral line (Fig.10). Similarly, for guiding magnetic fields $B_\parallel \lesssim 260$ G, the cyclotron upshift of the synchronous mode is too low to allow the coupling to the $TM_{11}$ fundamental mode, and no narrow band radiation is observed. At these low power levels, we are probably observing RF power generated via the negative-mass instability [19], and the radiation becomes broadband.

The relatively low power levels achieved in our device can be partially attributed to the following causes. Design limitations impose the use of an $N = 24$ periods wiggler field to excite radiation in the coaxial configuration (high cutoff frequency), resulting in a weak wiggler strength ($B_w \simeq 0.4$ kG). The theory [7] predicts that the interaction is very sensitive on the energy spread $\Delta\gamma/\gamma$; in our experiments, the use of a cold cathode limits our ability to achieve high beam quality with $\Delta\gamma/\gamma \sim 5\%$. The spatial growth curve (Fig.9) clearly indicates that most of the radiation is generated over a very short axial length of the wiggler ($\sim 2$ cm); beam deterioration may severely limit the efficiency achieved. Finally, it is not at all clear how efficiently the radiation is being coupled out of the system.

## V. CONCLUSIONS

The experimental studies indicate that the production of coherent microwave radiation by the interaction of a rotating relativistic electron ring with an azimuthally periodic wiggler field has been achieved in a manner consistent with theoretical expectations. The voltage tuning curves and the radiation pattern are consistent with single-mode operation in the coaxial waveguide configuration ($TM_{11}$). In particular, the agreement between the measured radiation frequency as a function of the beam voltage and the predicted values given by equation (6) is excellent. The radiation is narrowband ($\Delta\omega/\omega < 5\%$) and voltage-tunable over a wide frequency range ($\sim 50\%$, from 12.5 to 18 GHz). The coaxial waveguide configuration proves to yield higher power levels and more reproducible data, with a better control of both the electron orbits and the mode content than the hollow waveguide configuration.

## ACKNOWLEDGEMENTS

# References

[1] N.M. Kroll and W.A. McMullin, Phys. Rev. **A17**, 300 (1978)

[2] P.A. Sprangle, R.A. Smith and V.L. Granastein, *Infrared and Millimeter Waves*, edited by K.J. Button (Academic Press, New York, 1979), Vol. 1, p.279, references therein

[3] G. Bekefi, Appl. Phys. Lett. **40**, 578 (1982)

[4] R.C. Davidson, W.A. McMullin and K. Tsang, Phys. Fluids **27**, 233 (1984)

[5] C.L. Chang, E. Ott, T.M. Antonsen Jr. and A.T. Drobot, Phys. Fluids **27**, 2937 (1984)

[6] F. Hartemann, G.L. Johnston, G. Bekefi and R.C. Davidson, to be published

[7] H. Saïto and J. Wurtele, Phys. Fluids, to be published

[8] Y.Z. Yin and G. Bekefi, Phys. Fluids **28**, 1186 (1985)

[9] Y.Z. Yin, R.J. Ying and G. Bekefi, IEEE Jour. Quantum El. special issue on FELs, to be published

[10] F. Hartemann, G. Bekefi and R.E. Shefer, IEEE Trans. Plasma Science **13**, 484 (1985)

[11] G. Bekefi, R.E. Shefer and W.W. Destler, Appl. Phys. Lett. **44**, 280 (1984) ; also G. Bekefi, R.E. Shefer and B.D. Nevins, Laser'82 Conference Proceedings of the Society for Optical and Quantum Electronics (SOQUE, New Orleans, 1982), p.136

[12] W.W. Destler, F.M. Aghamir, D.A. Boyd, G. Bekefi, R.E. Shefer and Y.Z. Yin, Phys.

11

Fluids **28**, 1962 (1985)

[**13**] E. Chojnacki and W.W. Destler, IEEE Jour. Quantum El. special issue on FELs, to be published

[**14**] M.J. Rhee and W.W. Destler, Phys. Fluids **17**, 1574 (1974)

[**15**] W.W. Destler and M.J. Rhee, Phys. Fluids **20**, 1582 (1977)

[**16**] G.P. Scheitrum and R. True, Proceedings of the IEDM, 332 (1981)

[**17**] F. Hartemann and G. Bekefi, Appl. Phys. Lett. **49**, 1680 (1986)

[**18**] This familiar technique is described, for example in T.J. Orzechowski and G. Bekefi, Phys. Fluids **22**, 978 (1979)

[**19**] J. Swegle and E. Ott,Phys. Fluids **24**, 1821 (1981), references therein

# Figure captions

**Fig.1** Top : front view of the interaction region. Bottom : side view of the experimental arrangement.

**Fig.2** a) electron beam voltage ; b) total upstream diode current ; c) rotating (downstream) electron beam axial current ; d) microwave pulse in the X-band frequency range (8–12 GHz).

**Fig.3** Threshold voltage of the magnetic cusp as a function of the applied magnetic field. Insert : transmitted axial beam current as a function of the beam voltage ( $B_\parallel$ = 210 G is fixed). The arrow indicates the cusp threshold.

**Fig.4** a) Čerenkov measurements of the cross-section of the relativistic rotating electron ring with no wiggler field ; b) identical to a) for $N = 12$ wiggler periods, $B_w \simeq 0.8$ kG ; c) $N = 24$ wiggler periods, $B_w \simeq 0.4$ kG ; d) computer simulation of the electron orbits for $N = 12$.

**Fig.5** Relative angular RF power distribution $P(\theta)/P(\theta_0)$ for the hollow waveguide configuration ( $\omega_{c0} = 1.8$ GHz).

**Fig.6** Relative angular RF power distribution $P(\theta)/P(\theta_0)$ for the coaxial waveguide configuration ( $\omega_{c0} = 12.6$ GHz).

**Fig.7** Relative azimuthal RF power distribution $P(\phi)/P(\phi_0)$ in the hollow waveguide configuration.

**Fig.8** Relative output power as a function of the beam energy for 3 different values of the guide field $B_\parallel$ .

**Fig.9** Spatial growth of the RF power in the axial direction [ $P(z)/P(z_0)$ ].

**Fig.10** Voltage-tuning of the radiation frequency for 3 different values of the external magnetic field $B_\parallel$ . The experimental data is obtained from dispersive line measurements.

13

The solid lines are from theory [equation (6)].

**Fig.11** Schematic diagram of the interaction between a waveguide mode and a synchronous wave supported by the rotating electron beam. The $\omega^+$ and $\omega^-$ intersection points represent the upshifted and downshifted waves, respectively.
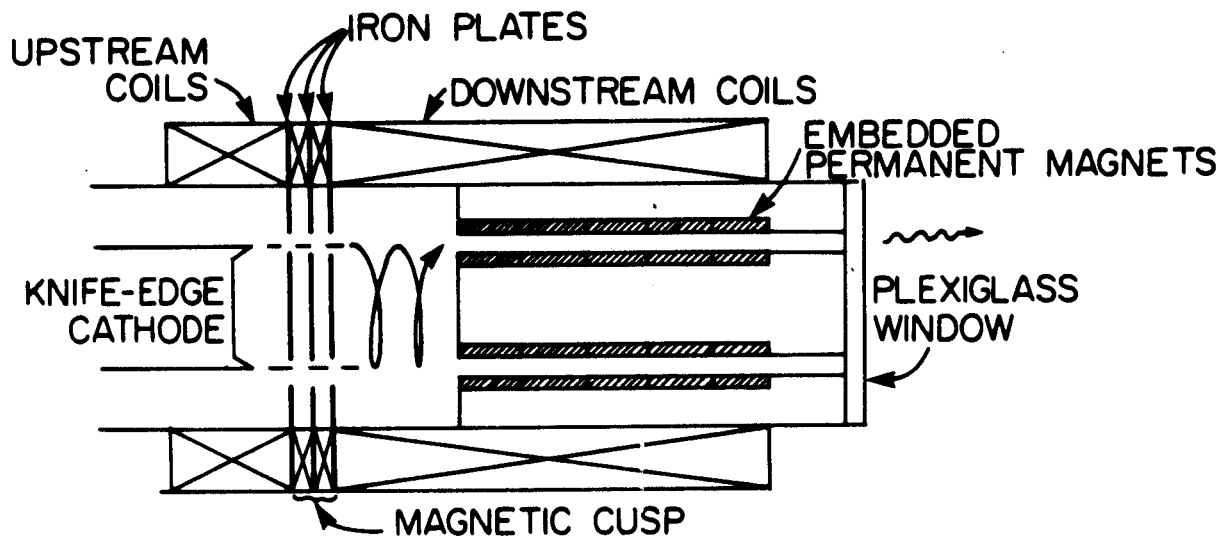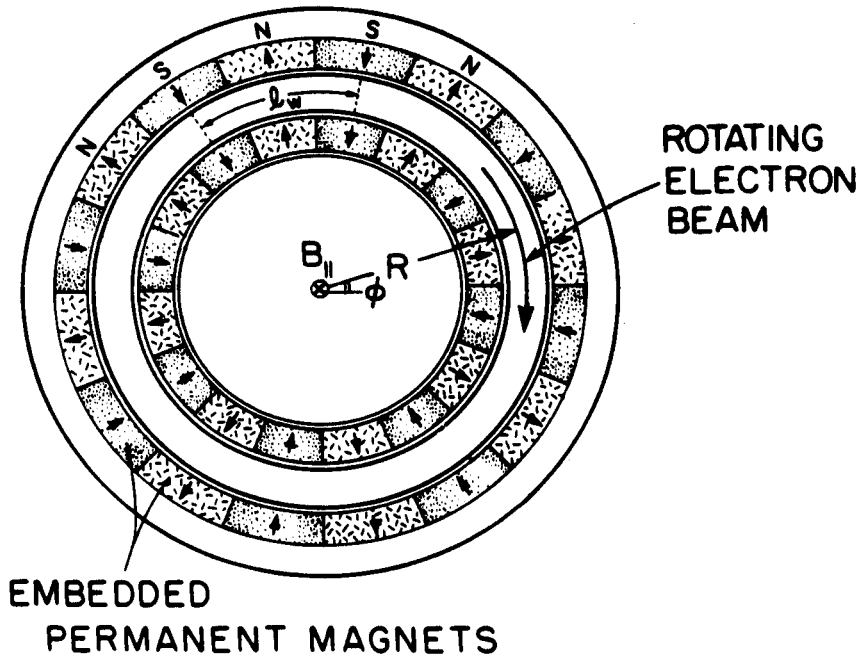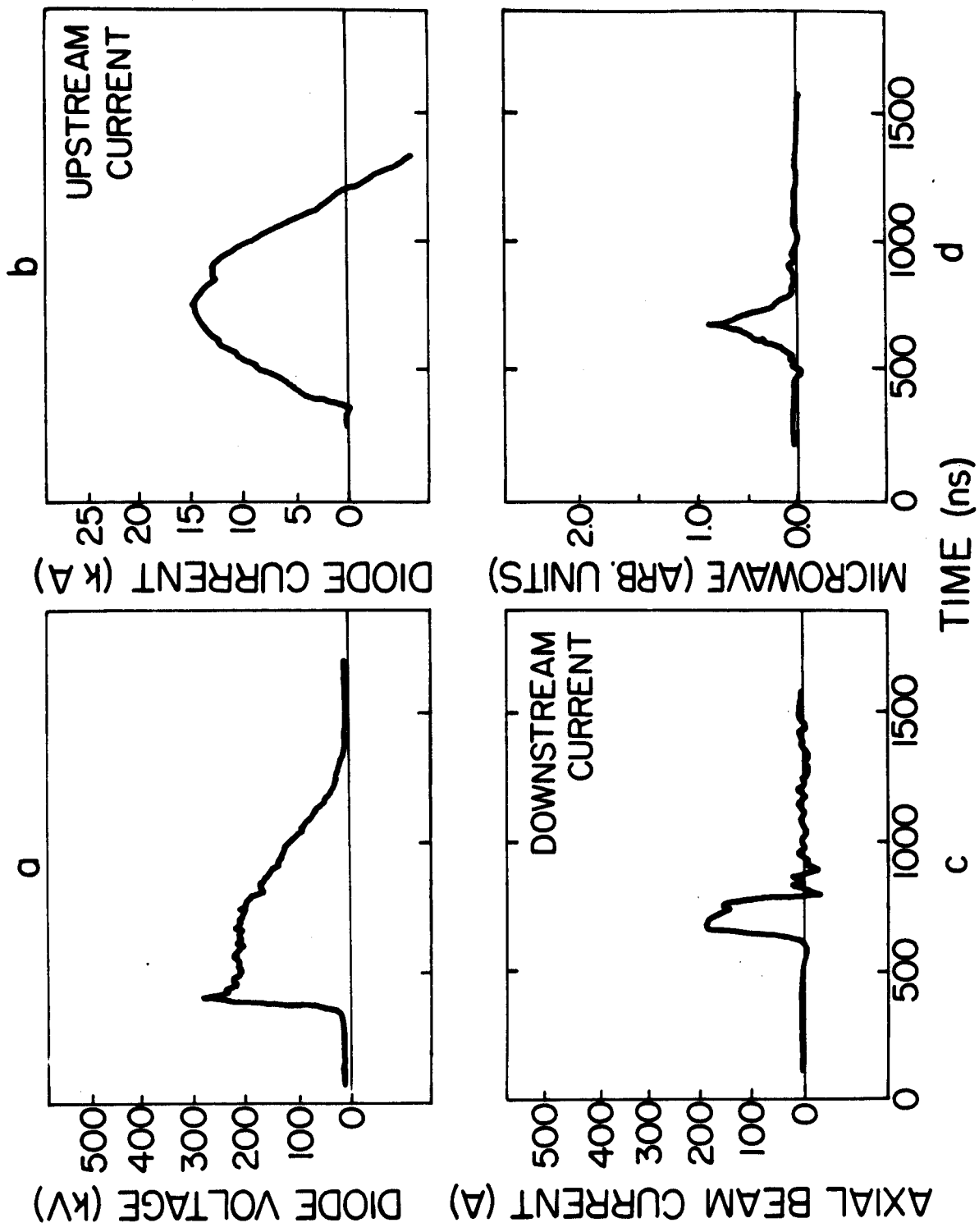
ROTATING
ELECTRON
BEAM

$B_{\parallel}$  $R$  $\phi$

EMBEDDED
PERMANENT MAGNETS

UPSTREAM
COILS

IRON PLATES

DOWNSTREAM COILS

EMBEDDED
PERMANENT MAGNETS

KNIFE-EDGE
CATHODE
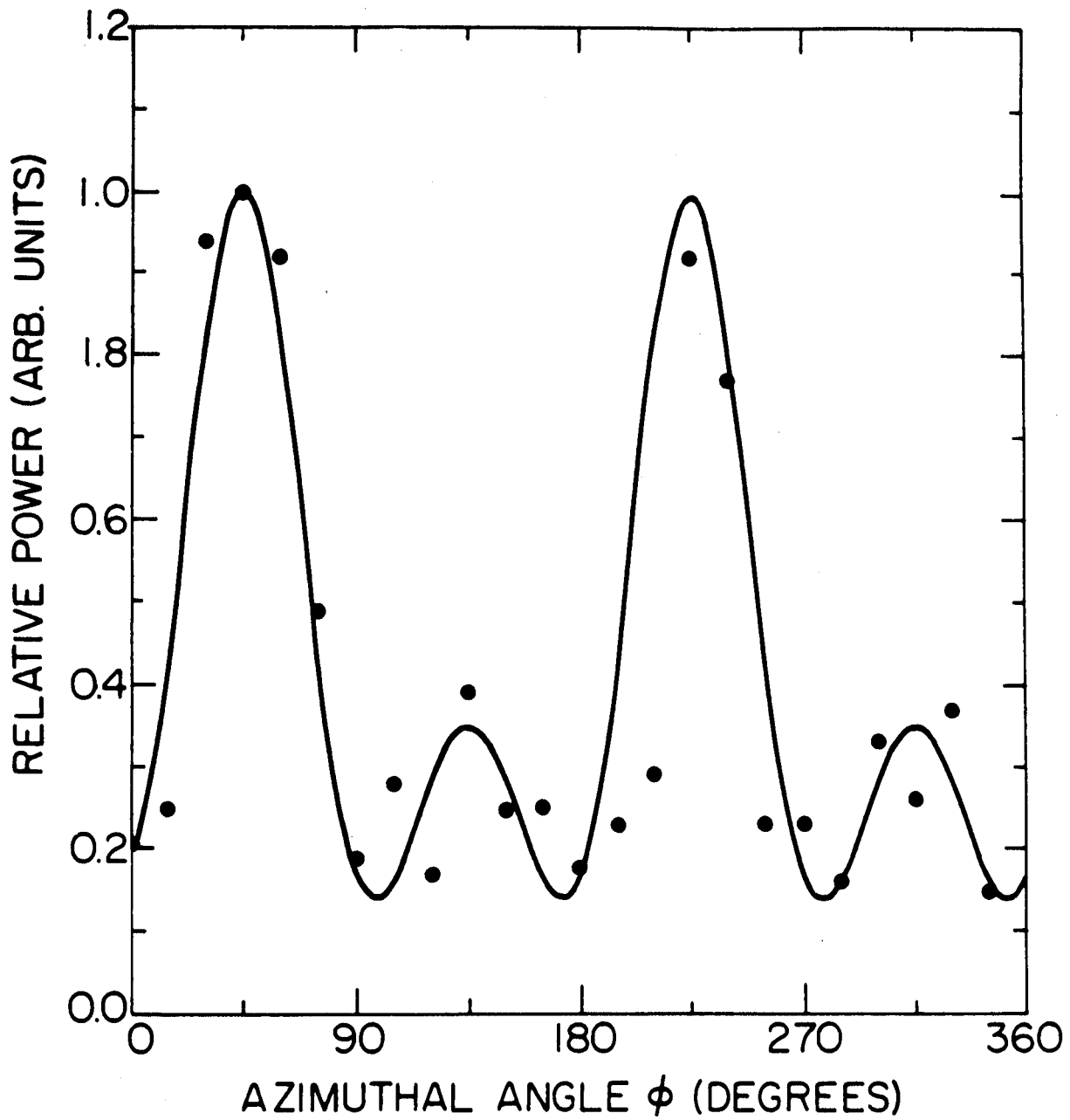
PLEXIGLASS
WINDOW

MAGNETIC CUSP

Fig. 1
Hartemann & Bekefi

Fig. 2
Hartemann & Bekefi
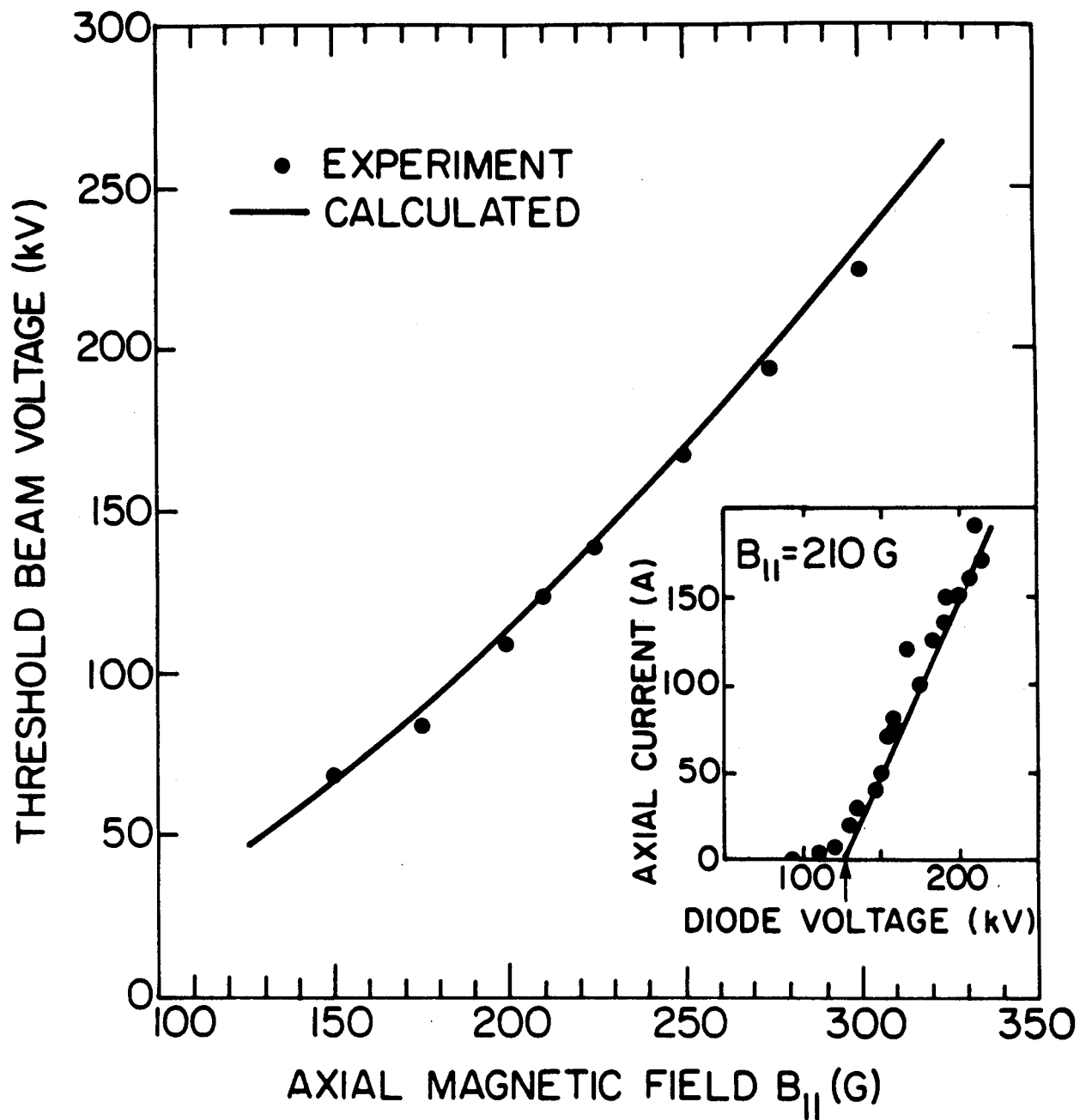
Fig. 3
Hartemann & Bekefi

a

b

c

cm
6.0

0.0

-6.0

-6.0        0.0        6.0 cm

d
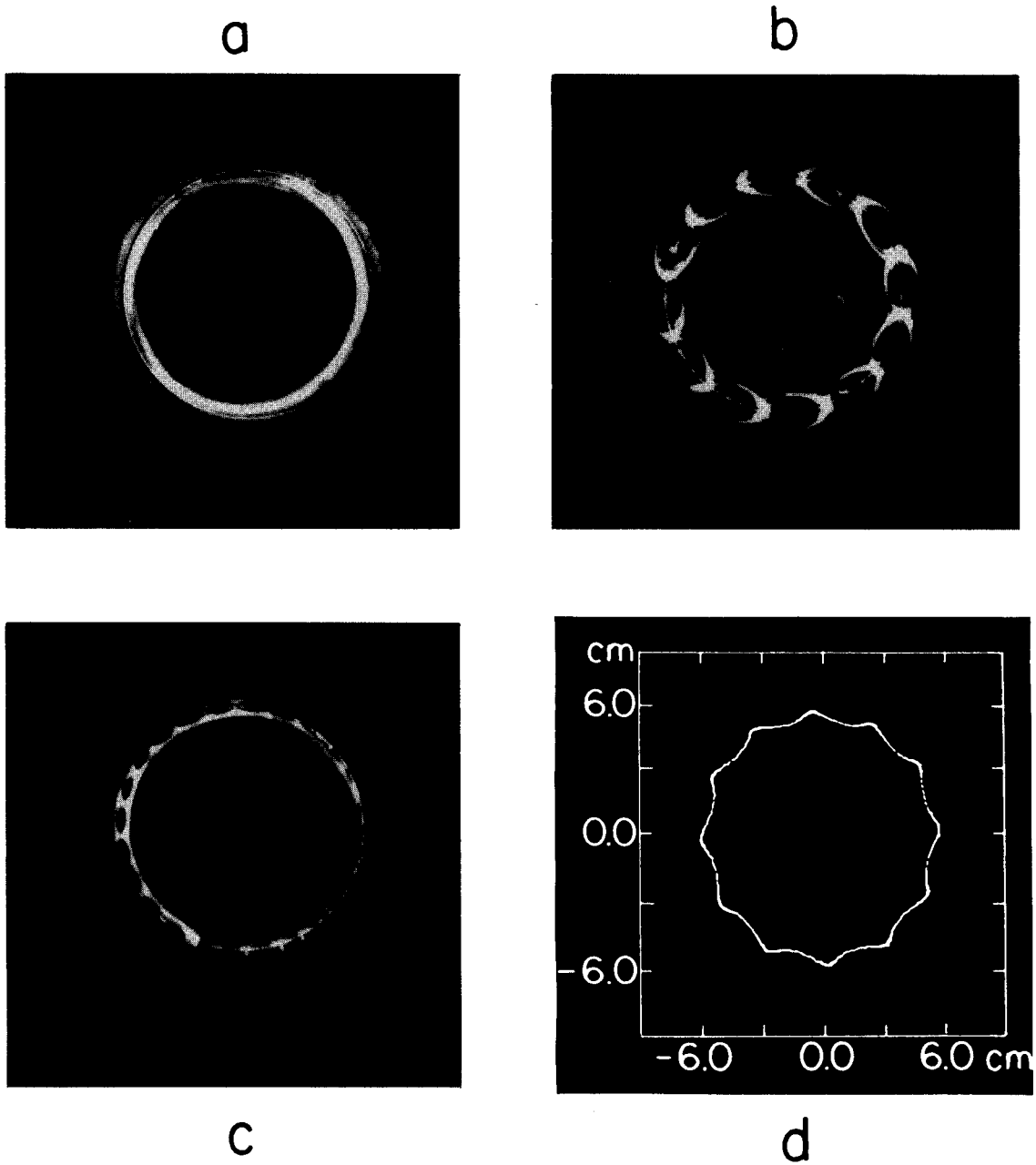
Fig. 4
Hartemann & Bekefi
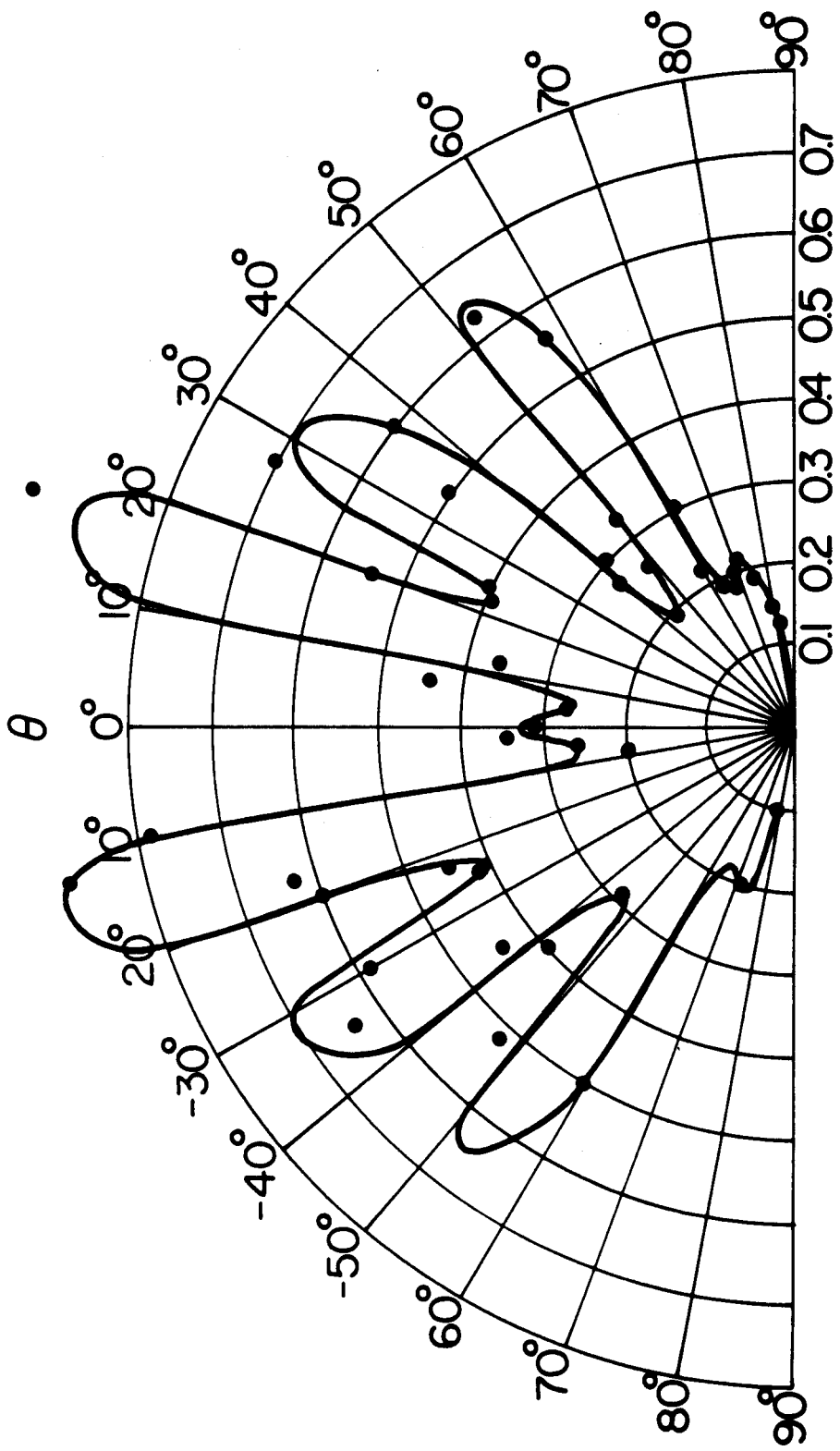
Fig. 5
Hartemann & Bekefi
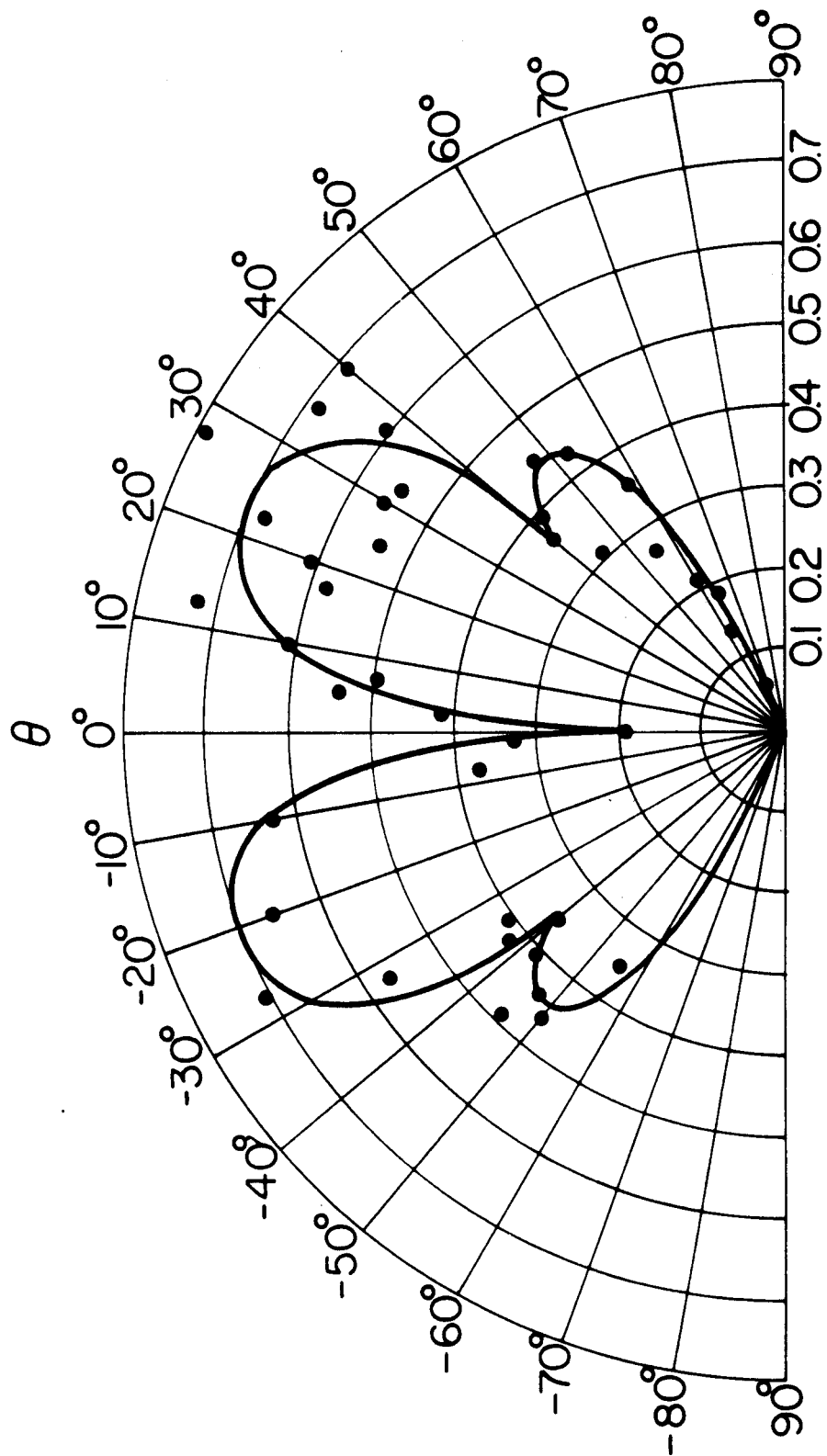
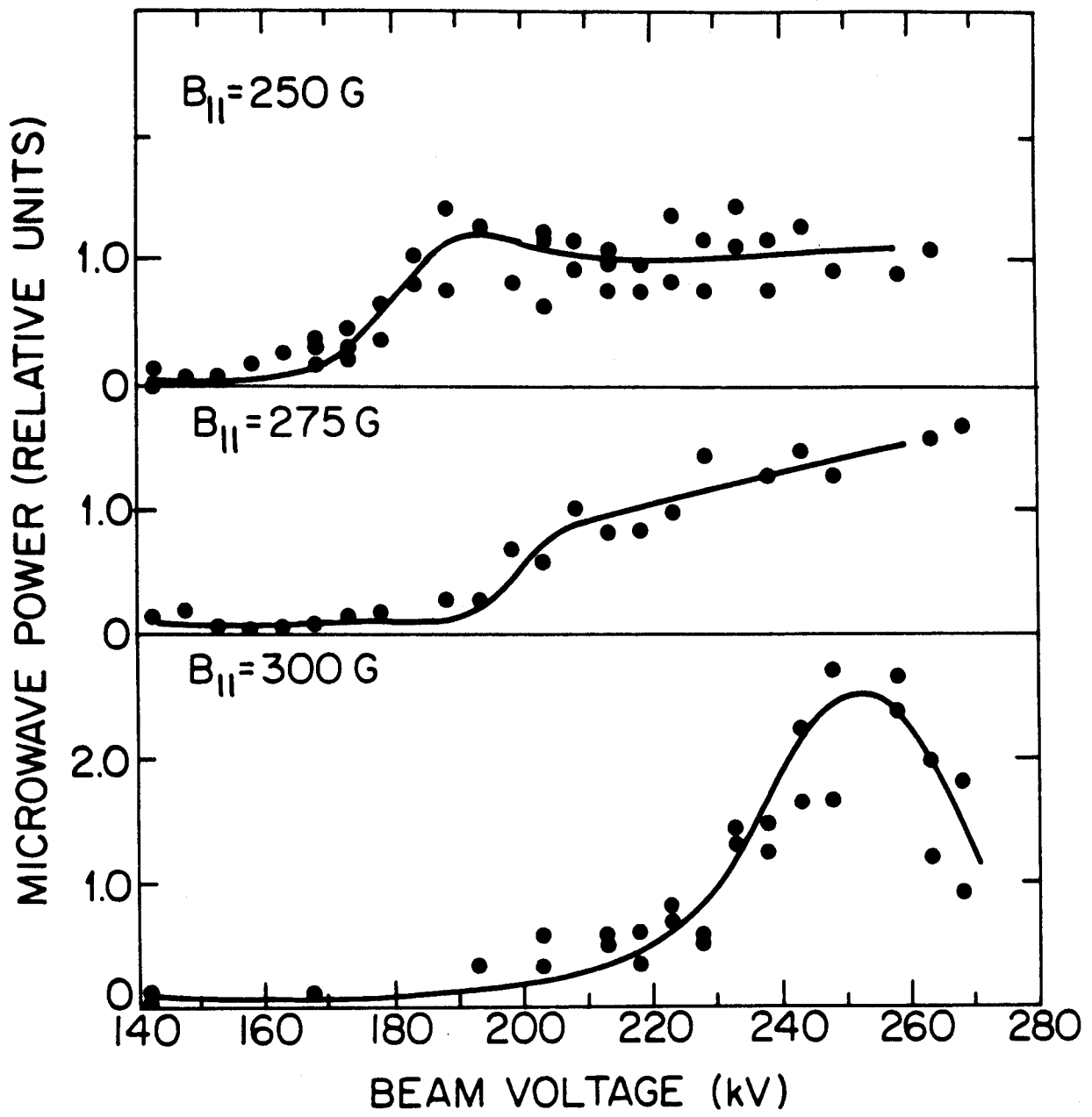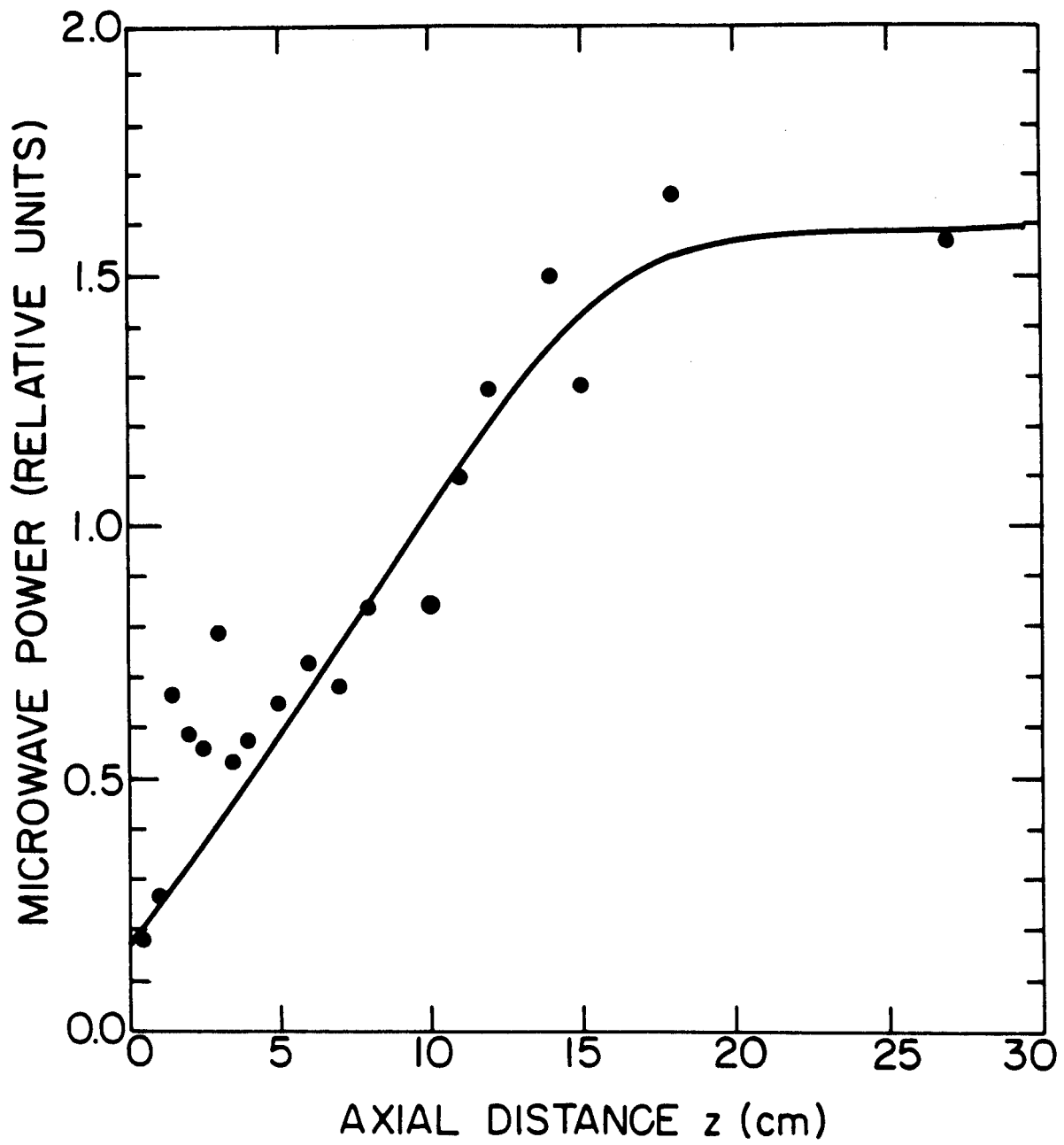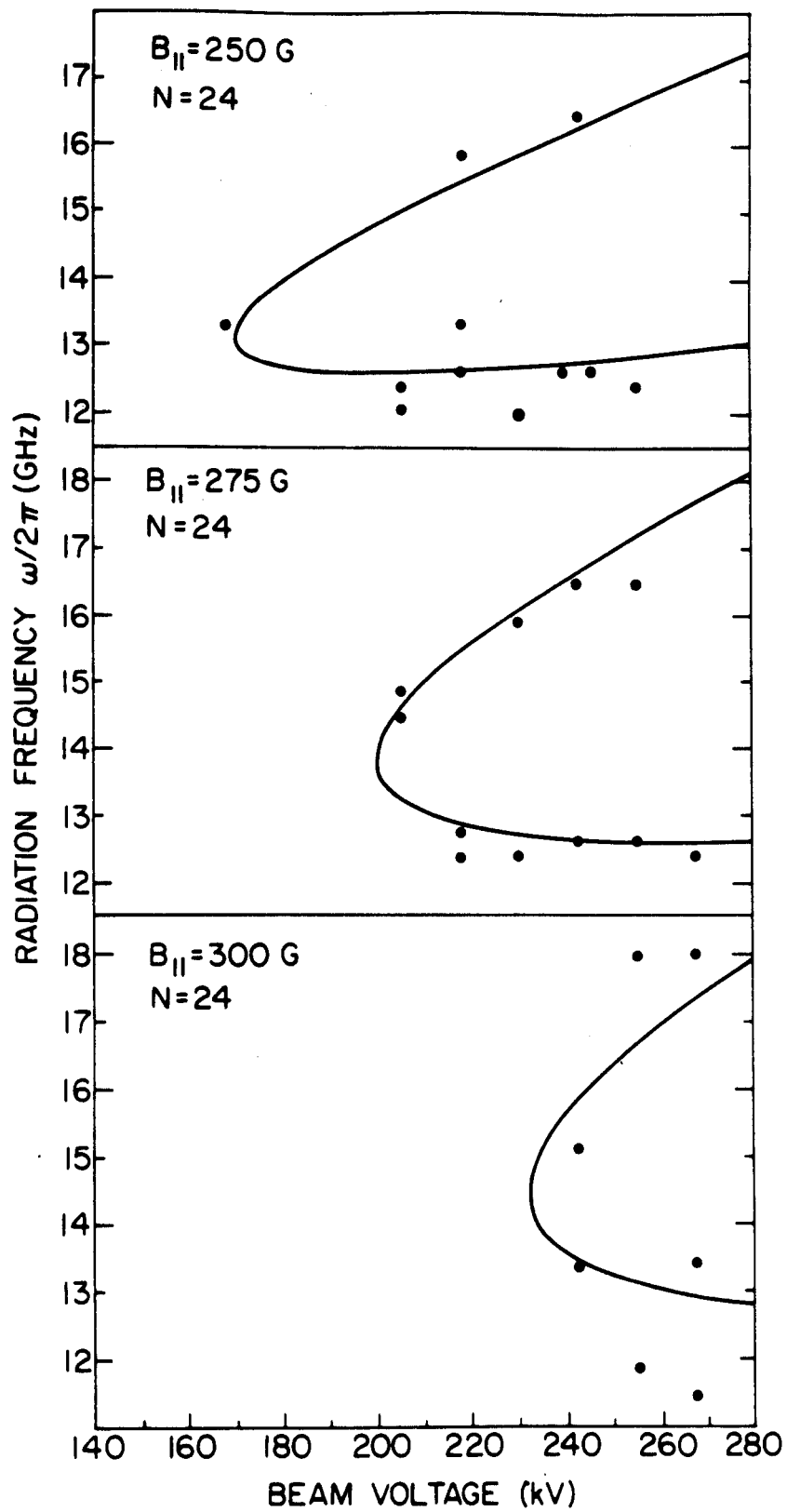Fig. 6
Hartemann & Bekefi

Fig. 7
Hartemann & Bekefi

Fig. 8
Hartemann & Bekefi

Fig. 9
Hartemann & Bekefi

Fig. 10
Hartemann & Bekefi

$TM_{\ell m}MODE$

$\omega^2 = \omega_c^2(\ell,m) + k_\parallel^2 c^2$

$\omega = (\ell+N)\Omega_\parallel + k_\parallel V_\parallel$
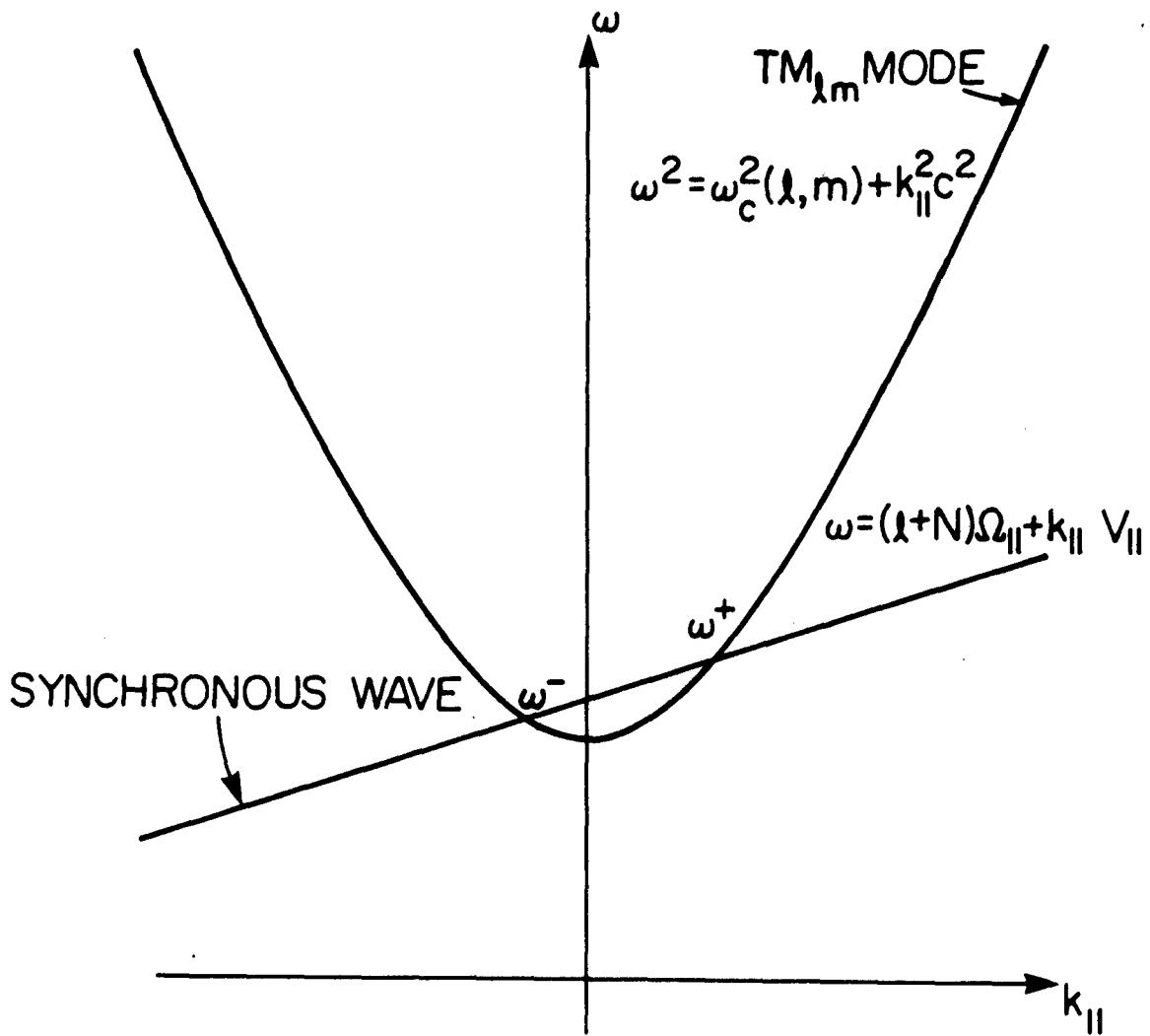
$\omega^+$

$\omega^-$

SYNCHRONOUS WAVE

$\omega$

$k_\parallel$

Fig. 11
Hartemann & Bekefi